

# Properties of arrays of microplasmas: application to control of electromagnetic waves

Chenhui Qu<sup>1</sup> , Peng Tian<sup>1</sup> , Abbas Semnani<sup>2</sup>  and Mark J Kushner<sup>1,3</sup> 

<sup>1</sup> University of Michigan, Department of Electrical Engineering and Computer Science 1301 Beal Ave., Ann Arbor, MI 48109-2122, United States of America

<sup>2</sup> Purdue University, School of Electrical and Computer Engineering, West Lafayette, IN 47907, United States of America

E-mail: [chenqu@umich.edu](mailto:chenqu@umich.edu), [tianpeng@umich.edu](mailto:tianpeng@umich.edu), [asemnani@purdue.edu](mailto:asemnani@purdue.edu) and [mjkush@umich.edu](mailto:mjkush@umich.edu)

Received 20 July 2017, revised 8 September 2017

Accepted for publication 18 September 2017

Published 3 October 2017



## Abstract

Microplasma arrays (MAs) are being investigated as a method to control the propagation of electromagnetic waves. The use of MAs as an electromagnetic wave controlling material is attractive as the electrical properties of MAs can be rapidly changed through combinations of the choice of operating conditions (e.g. pressure, gas mixture), the spatial distribution of the plasma and applied voltage waveforms. In this paper, results from a computational investigation of the plasma properties of small arrays of microplasmas are discussed. The model systems are arrays of microplasmas sustained in rare gases at pressures of up to 100 Torr in a sealed chamber. Individual plasma cells are  $\approx 100 \mu\text{m}$  in size. Pulsed dc voltage waveforms having widths of 30 ns are applied at repetition rates of up to 10 MHz. The cross-talk between plasma cells was investigated, as well as the consequences of gas heating and sequencing of the pulses. We found that even without physical barriers between the plasma cells to control cross-talk between cells, the individual character of each cell can be retained; however the plasma cells were not completely independent. The diffusion of metastable excited atomic states and small fluxes of ions did enable adjacent cells to operate at lower voltages. The ability to control microwave propagation through waveguides was computationally investigated by placing a MA inside a standard waveguide and examining the resulting transmission coefficients. We found that for frequencies of tens to 100 GHz, the transmitted power could be controlled by the spatial distribution of the MA cells with respect to the modal structure of the wave.

Keywords: microplasma, arrays, modeling, electromagnetic wave control

## 1. Introduction

The use of microplasmas to control the propagation of micro- and millimeter electromagnetic waves is motivated by the ability to control the properties of the plasmas, and their ability to interact with electromagnetic (EM) waves, over large dynamic ranges [1–6]. Microplasma arrays (MAs) are particularly attractive for controlling EM waves as the properties of individual plasma cells in the arrays can, in principle, be controlled, thereby providing the ability to customize the

spatial distribution of the plasma-EM wave interaction. The ability of plasmas to control the properties of EM waves results from a combination of the electron density and electron collision frequency, which in turn specifies the complex permittivity of the plasma. For example, the ratio of the plasma frequency to the EM frequency in part determines whether the EM wave can propagate through the plasma or is reflected.

Plasmas are generally a member of a class of materials whose refractive index and permittivity,  $\epsilon_p$ , can be less than unity and even negative (negative index material (NIM)). NIMs based on arrays of plasmas are being investigated as

<sup>3</sup> Author to whom correspondence should be addressed.

metamaterials and photonic crystals [7, 8]. Plasmas can naturally operate with a negative  $\varepsilon_p$  if the plasma frequency is greater than the frequency of the EM wave (in low-pressure regimes). Other than forming a metamaterial, plasmas having negative  $\varepsilon_p$  can be used as a reflector of EM waves.

Both kinds of aforementioned materials require large electron densities. The effective relative permittivity of the plasma is

$$\varepsilon_p = 1 - \frac{\omega_p^2}{\omega^2 \left(1 + \frac{j\nu_m}{\omega}\right)} = 1 - \frac{\omega_p^2}{(\omega^2 + \nu_m^2)} + j \frac{\omega_p^2 (\nu_m/\omega)}{(\omega^2 + \nu_m^2)}, \quad (1)$$

$$\omega_p = \sqrt{\frac{q^2 n_e}{\varepsilon_0 m_e}}, \quad (2)$$

where  $\omega = 2\pi f$  is the angular frequency of the incident EM wave having frequency  $f$ ,  $\omega_p$  is the electron plasma frequency,  $n_e$  is the electron density,  $\nu_m$  is the electron momentum transfer collision frequency,  $m_e$  is electron mass,  $\varepsilon_0$  is the vacuum permittivity and  $q$  is the elementary charge. The electron density and collision frequency are the controllable plasma properties that determine the electromagnetic properties of the plasma. Among the different combinations of  $\nu_m$  and  $\omega_p$ , some produce negative values of  $\varepsilon_p$ —for example,  $\omega_p^2 > \nu_m^2 + \omega^2$ , a criterion well satisfied for small  $\nu_m$  and  $\omega$  compared to  $\omega_p$ . A high plasma frequency results from a high electron density. So as an example, to make  $\varepsilon_p$  negative for a 20 GHz wave, an electron density of  $>10^{13} \text{ cm}^{-3}$  is required for pressures of 30–80 Torr.

The interaction between plasma arrays and EM waves has been experimentally and numerically investigated by several research groups. The interaction between EM waves and a MA generated in a double-split-ring resonator (DSRR) configuration was investigated by Iwai *et al* [9]. The non-linearity of the MA produced a second-harmonic-wave which provided the basis of using MAs as harmonic generators. The phenomenon of anomalous wave propagation caused by plasma array metamaterials was numerically investigated by Sakai [10]. Microplasma and larger arrays have been investigated for use as photonic-crystal-like materials. These studies were typically for EM waves whose wavelength is larger than the distance between microplasma elements [11–13]. Ideally, the distance between microplasma elements should be smaller than the EM wavelength so that statistical changes in the spatial distribution of the plasma do not significantly affect the EM interaction [4, 14].

To achieve the desired plasma properties, MAs are often generated by microwave excitation [1, 15, 16]. For example, MAs consisting of microstrip split ring resonators, DSRR and other microstructures with electric field enhancement in narrow gaps have been demonstrated at microwave frequencies [15–17]. If the plasma is generated by separate sets of electrodes, microplasma elements can be individually controlled by regulating the input power of the electrodes. This is, in fact, the basis of plasma display panels (PDPs)—control the intensity of the UV light striking phosphors by

combinations of voltage or repetition rate applied to each plasma cell [18]. Typical PDPs, however, are not optimum for control of EM waves, as they operate at electron densities that are too low and pressures (and collision frequencies) that are too high.

The application of MAs as a means to control electromagnetic wave propagation will depend on the ability to control the electron densities, collision frequencies and physical layout of the microplasma elements. To modulate the properties of EM waves, one is motivated to operate the plasma elements at high electron density and low gas pressure. Due to their small size (less than hundreds of microns), Paschen's law considerations imply that MAs must operate at high pressures. Unfortunately, large values of pressure produce large values of  $\nu_m/\omega$ , which then requires large electron densities to maintain conductivity. Operating at low pressures typically reduces the peak electron density that can be produced, and so results in a less negative (or more positive) real part of  $\varepsilon_p$ . Unlike commercial PDPs and other MAs intended for illumination, the structure of MAs for manipulation of EM waves should be as open as possible with little, if any, intervening materials between the plasma elements to minimize absorption and scattering of the EM wave. This open architecture is not a common design [19] may present challenges in controlling individual plasma elements in the MA. However, open designs of MAs are beginning to appear [20].

In this paper, we discuss results from a computational investigation of small arrays of microplasmas with the goal of demonstrating control of  $\varepsilon_p$  in open structures. The open structures are intended to be as transparent as possible to the EM wave when the MA is off. However, the open structure then enables cross-talk between the microplasma elements. The cross-talk, though not necessarily a negative, should also be controlled or at least characterized. We found that operational control of both the electron density and collision frequency is complicated by gas heating which rarefies the gas near the cathode of the microplasma element, which in turn affects the distribution of the plasma. With there being few physical barriers between the plasma cells, cross-talk does occur between the cells. Even though the cross-talk does not significantly affect the steady state operation of the plasma cells, the cross-talk does influence the startup characteristics of neighboring cells. The ability to control microwave transmission through waveguides was computationally demonstrated by inserting a MA into a commercial waveguide. We found that the physical layout of the microplasma elements could be used as a means to control transmission through the waveguide due to the overlap between the microplasma elements and the modal structure of the EM field in the waveguide.

The models used in this investigation are discussed in section 2. Results from the simulation for MA properties while varying voltage, gas mixture, pressure and layout of the MA are discussed in section 3. Predicted properties for control of EM wave transmission through waveguides using MAs are discussed in section 4. Our concluding remarks are in section 5.

## 2. Description of models

The model used in this investigation of properties of MAs is the Hybrid Plasma Equipment Model (HPEM), which is described in detail in [21]. In the HPEM, physical phenomena are grouped into modules which are sequentially executed in a time-slicing manner. In this work, the fluid kinetics module (FKM) and electron energy transport module (EETM) were used. In the FKM, the continuity, momentum and energy equations for all heavy particles are integrated in time coincident with Poisson's equation for the electric potential. For electrons, densities are provided from the electron continuity equation using a Shaffetter–Gummel formulation for the electron fluxes, and the electron temperature is provided from integration of the electron energy transport equation. Electron impact rate coefficients and transport coefficients are provided by stationary solutions of Boltzmann's equation.

The transport of secondary electrons emitted from surfaces, and the cathode in particular, are important to the operation of the microplasma devices due to their acceleration in the bounding sheaths. Electron energy distributions and transport coefficients for secondary electrons emitted from surfaces are provided by the EETM in which an electron Monte Carlo simulation (eMCS) is used to follow their trajectories and collisions. The eMCS is described in [22]. Spatially dependent electron energy distributions are produced from the eMCS, which then provides electron impact source functions for inelastic collisions.

Electromagnetic transmission through waveguides loaded with MAs was modeled with the commercial simulation package ANSYS Electromagnetics [23]. The material of the waveguide was copper and the wave port option was used as the excitation method on both ends of the waveguide. The plasma elements within the waveguide were defined as a material having real and imaginary components of the permittivity. For EM angular frequency  $\omega$ ,

$$\text{Re}(\varepsilon_p) = \frac{\varepsilon_0 m_e (\omega^2 + \nu_m^2) - e^2 n_e}{\varepsilon_0 m_e (\omega^2 + \nu_m^2)}, \quad (3)$$

$$\text{Im}(\varepsilon_p) = \frac{-e^2 n_e \nu_m}{\omega \varepsilon_0 m_e (\omega^2 + \nu_m^2)}. \quad (4)$$

The results from the HPEM were used for values of  $n_e$  and  $\nu_m$ . For ease of computation, each plasma element of the array in the ANSYS simulations was approximated as having uniform plasma properties. The permittivity of these identical plasma elements was calculated based on the values of  $n_e$  and  $\nu_m$  from the HPEM, and the frequency of the input EM wave. The finite element method in ANSYS was used to address the EM wave propagation. The scattering (S) parameter matrix was calculated on each port to monitor power flow into and out of the waveguide.

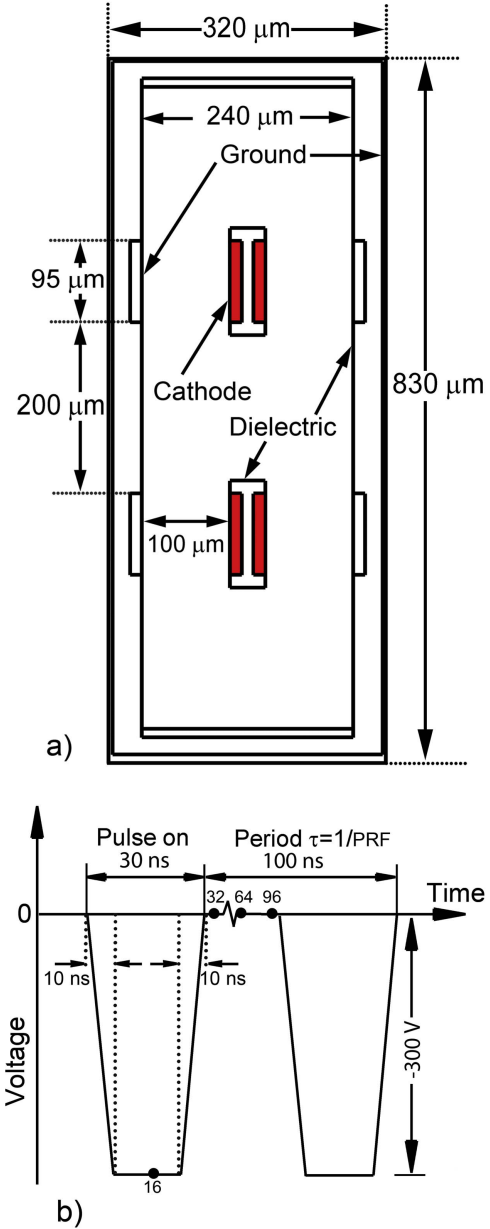


**Figure 1.** Conditions for the base case. (a) Geometry and (b) voltage wave form. The dots at 16, 32, 64 and 96 ns approximately indicate the times at which images are shown in figure 2.

## 3. Plasma characteristics of small arrays of microplasmas

The base case geometry for these studies is shown in figure 1(a). The micro-chamber contains four pairs of electrodes arranged in a  $2 \times 2$  array intended to produce individual quasi-independent microplasmas. Cathodes are located on the centerline of the chamber while grounded anodes are recessed in the dielectric walls. Both the cathodes and anodes are exposed to the plasma. This arrangement of electrodes resulted from a parametric study which showed that there was less cross-talk between microplasmas with the anode recessed in the wall instead of the cathode. The electrodes are 95 μm wide and separated by 200 μm with a cathode–anode electrode separation of 100 μm. The micro-chamber is sealed (that

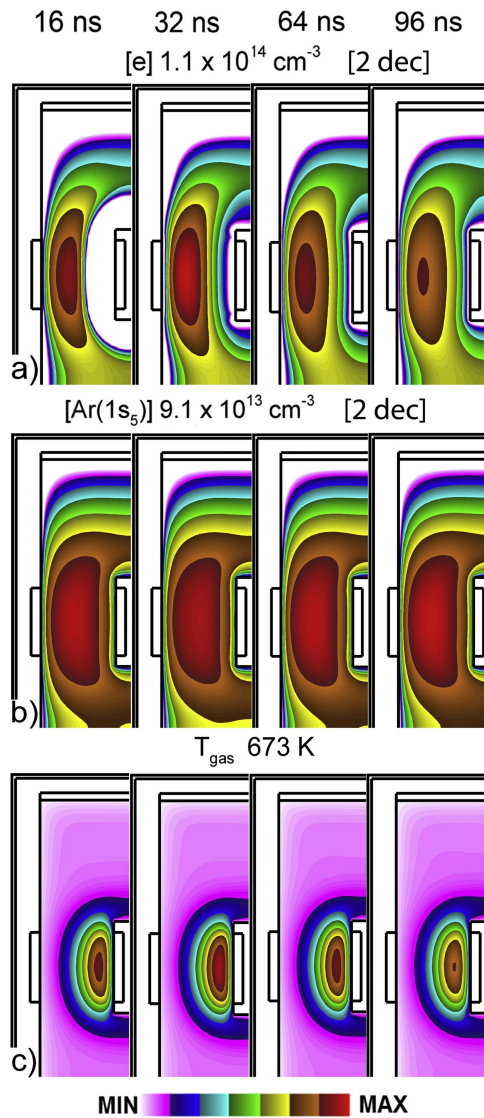


**Figure 2.** Plasma properties in a  $2 \times 2$  array for the base case (Ar, 60 Torr,  $-300$  V) for different times during the voltage pulse approximately shown in figure 1. The plasma is the same in all cells and so only the top left cell is shown. (a) Electron density, (b) Ar( $1s_5$ ) density and (c) gas temperature. The voltage pulse ends at 30 ns.

is, no gas inlet or pumping) so the usual pressure boundary condition is replaced by requiring that the total inventory of atoms remains constant (for rare gases). The outer boundary is grounded metal. The total width of the micro-chamber is  $320 \mu\text{m}$  and the total length is  $830 \mu\text{m}$ .

The applied voltage waveform is shown in figure 1(b). In the base case, the pulse repetition frequency (PRF) is 10 MHz and the duty-cycle is 30%, translating to a period of 100 ns with a pulse-on time of 30 ns. The rise and fall times of the voltage are 10 ns. The voltage pulses are unipolar with an amplitude of  $-300$  V. Pure Ar is the operating gas in the base case. The reaction mechanism is the same as discussed in [24]. The secondary electron emission coefficient for ions striking the cathode was 0.15 [25].

The electron density, the metastable Ar( $1s_5$ ) density and gas temperature are shown in figure 2 during the pulsed cycle

for the top-left cell of the MA. Voltage is simultaneously applied to the cathodes of all four cells. The electron impact ionization source by bulk electrons and by secondary electrons emitted from the cathode, total power deposition and electron temperature are shown during the pulsed cycle in figure 3. These results are shown after 30 pulses, which is sufficient to achieve a pulse-periodic steady state. The peak values of ionization are approximately the same by bulk electrons and secondary electrons emitted from the cathode. However, when integrated over the entire device, ionization is dominated by the high energy secondary electrons. The mean free path of secondary electrons having an energy of 300 eV, assuming the secondary electrons are collisionlessly accelerated across the cathode fall, is  $\approx 56 \mu\text{m}$ . This distance is commensurate with the cathode–anode spacing, and so ionization extends across the entire gap. This results in some beam electrons being collected by the anode. The electron temperature in the bulk plasma (shown in figure 3 outside of the cathode fall) is about 3.5 eV.

The peak plasma density,  $1.1 \times 10^{14} \text{ cm}^{-3}$ , produces a cathode fall thickness of  $\approx 45 \mu\text{m}$  which occupies about half of the cathode–anode gap. The edge of the cathode fall is indicated by the boundary of the bulk electron density surrounding the cathode. The curvature of this boundary (and some scattering of the secondary electrons) produces only a moderate amount of ionization that extends beyond the edge of the cathode. Other than the exclusion of electrons from the growing and collapsing cathode fall, there is little variation in the electron density during the 100 ns period. The comparatively thick cathode fall results in there being two peaks to the ionization by bulk electrons—in the bulk plasma and at the edge of the cathode fall. The latter source results from electrons produced from ionization by beam electrons, which are then accelerated in the sheath. The secondary electrons also efficiently produce excited states, an example being the density of Ar( $1s_5$ ) having a maximum value of  $9 \times 10^{13} \text{ cm}^{-3}$ . Power deposition peaks in the cathode fall, indicating that the major contribution is from ion acceleration with a local peak of  $450 \text{ kW cm}^{-2}$ . The resulting increase in gas temperature is to 670 K. In this pulse periodic steady state, the gas temperature oscillates by only a few degrees during the cycle.

In spite of there being no physical barrier in the MA chamber to isolate the plasma cells (other than the cathodes), the individual micro-plasmas in this  $2 \times 2$  array are still fairly distinct with only weak cross-talk. For example, the electron, Ar $^+$  and Ar( $1s_5$ ) densities in the full array are shown in figure 4 at the end of the voltage pulse. These distinct plasmas are in part enabled by ionization having a large component due to secondary electrons emitted from the cathode. These electrons are geometrically constrained to the cathode–anode gap, in spite of there being fringing electric fields at the edge of the cathode. The ionization by bulk electrons could, in principle, occur over a larger physical extent of the micro-chamber, as electron energy is convected by the high thermal conductivity of the plasma. However, by having short pulses, the power transfer by thermal conduction or convection can be contained, and so maintain the integrity of the individual



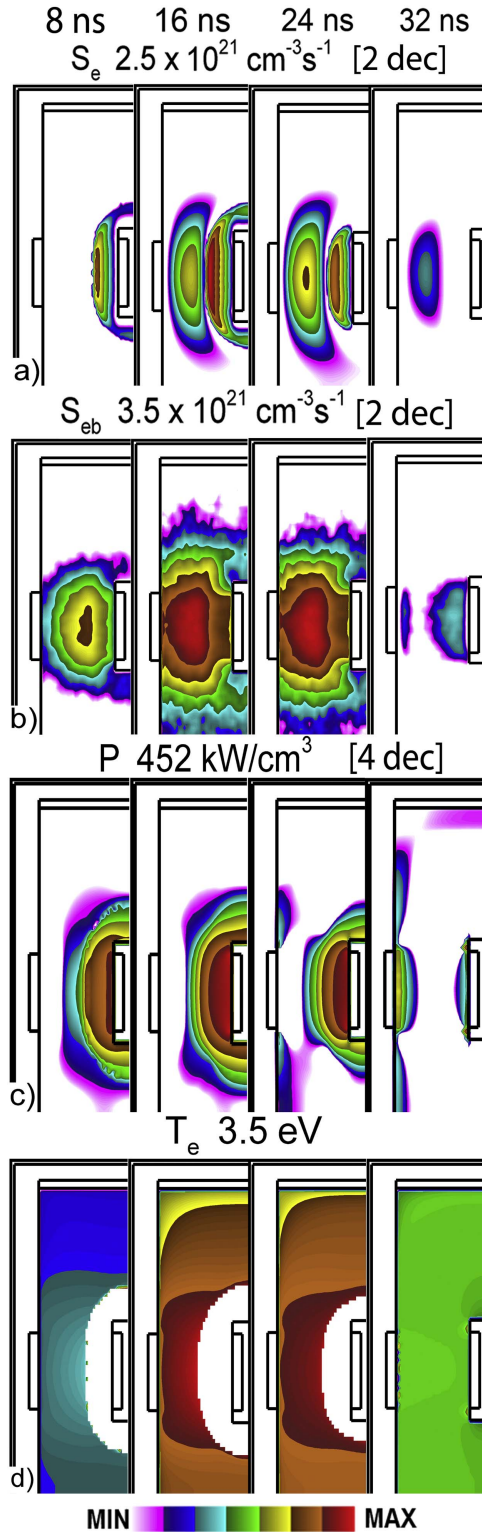


**Figure 3.** Plasma properties in a  $2 \times 2$  array for the base case (Ar, 60 Torr,  $-300$  V) for different times during the voltage pulse. The plasma is the same in all cells and so only the top left cell is shown. Electron impact ionization source by (a) bulk electrons and (b) secondary electrons emitted from the cathode, (c) total power deposition and (d) electron temperature. The electron temperature is plotted only outside the cathode fall.

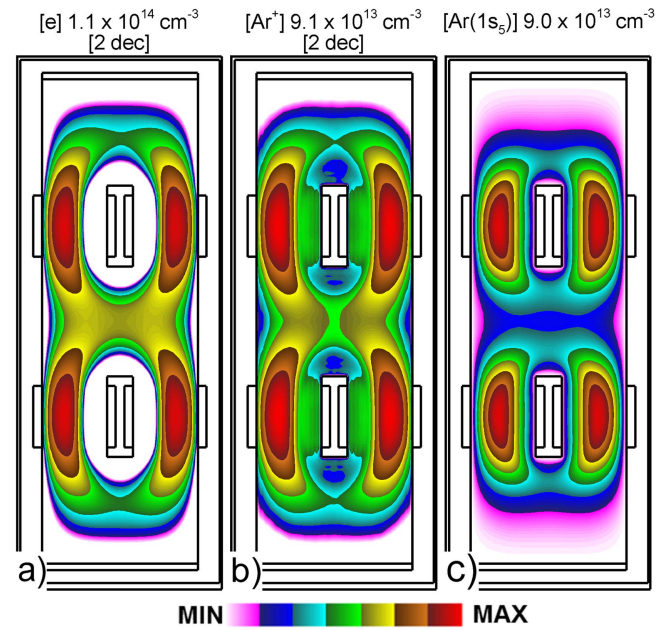


**Figure 4.** Distribution of (a) electron density, (b)  $\text{Ar}^+$  density and (c) density of  $\text{Ar}(1s_5)$  in a  $2 \times 2$  array.

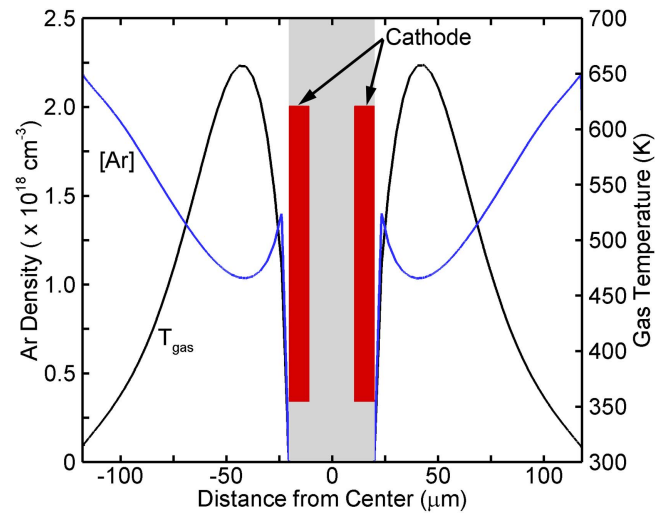


**Figure 5.** Distributions of gas temperature and Ar density at mid-electrode in the  $2 \times 2$  array.

cells. The characteristic time for heating and energy dissipation at 60 Torr is short compared to the length of the 30 ns voltage pulse; whereas the time for electron thermal conduction between cells is long compared to the 30 ns voltage pulse. So maintaining a short voltage pulse minimizes cross-talk between the cells.

The peak power density,  $450 \text{ kW cm}^{-3}$ , results in substantial gas heating, as shown in figure 5, where the gas temperature and Ar density are shown perpendicular to the center of the cathode. Although in an actual device, the surfaces in contact with the plasma will heat, surfaces here are constrained to remain at 300 K. Since the time for thermal

conduction through the argon gas is long compared to the interpulse period, the gas temperature increases on a pulse-to-pulse basis to this profile. Although there is some small modulation in the gas temperature during the pulsed cycle, the profile shown in figure 5 is essentially a steady state value achieved by small increments over 30 pulses. The gas heats to a peak of more than 650 K near the edge of the cathode fall, producing a rarefaction the density of Ar by a factor of 2 from the nominal fill density of  $1.9 \times 10^{18} \text{ cm}^{-3}$  (60 Torr, 300 K). Since this is a sealed device, the total inventory of Ar atoms is conserved and so rarefaction in one region of the device produces a higher density elsewhere. The rarefaction, largely in the cathode fall, produces an increase in density in the bulk plasma. This situation is favorable to producing ionization by secondary electrons and to isolating the MA elements. The rarefaction near the cathode produces a longer mean-free-path for secondary electrons to gain the maximum possible energy. The increased gas density beyond the cathode fall provides more efficient stopping of those more energetic electrons. The larger gas density outside the ionization region slows the thermal conduction of electron energy, thereby helping to confine the individual MA elements.

### 3.1. Peak voltage

The spatial scalings of MA properties (electron density, gas temperature and secondary electron ionization source) with peak voltage are shown in figure 6. All other operating parameters are the same as the base case. The electron density, gas temperature and ion density as a function of applied voltage are shown in figure 7 at the location and time of the maximum electron density during the pulsed cycle. In each case, the spatial distribution of the four active plasma regions in the micro-chamber have the same scaling, and so only one cell is shown for each voltage. With increasing voltage, the plasma density and peak gas temperature increase roughly in proportion to the voltage while the cathode fall thickness increases due to the higher cathode potential. The increasing cathode fall thickness for a finite cathode length also produces some curvature in the edge of the cathode fall, resulting in electric field vectors that diverge from being perpendicular to the cathode. With a thin cathode fall across the flat cathode, the sheath appears to be one-dimensional. As the cathode fall thickens with increasing voltage, the edge of the cathode fall gains curvature with electric field vectors no longer perpendicular to the cathode as the cathode subtends a smaller angle. The end result is that there is a more broadly distributed source of ionization by secondary electrons, which then increases the cross-talk between plasma cells. This increasing amount of cross-talk is indicated by the merging of the plasmas for each individual cell with their neighbors at the higher voltages.

Although the electron density does increase with increasing voltage, to a maximum value of  $1.5 \times 10^{14} \text{ cm}^{-3}$  at  $-400 \text{ V}$ , the rate of increase decreases with increasing voltage. First, the compression of the bulk plasma by the thickening of the cathode fall produces less efficient ionization by bulk electrons by lowering the electron temperature. Second, ionization is reduced due to gas heating. The increase in power deposition with increasing voltage produces an increase in the peak gas temperature—up to

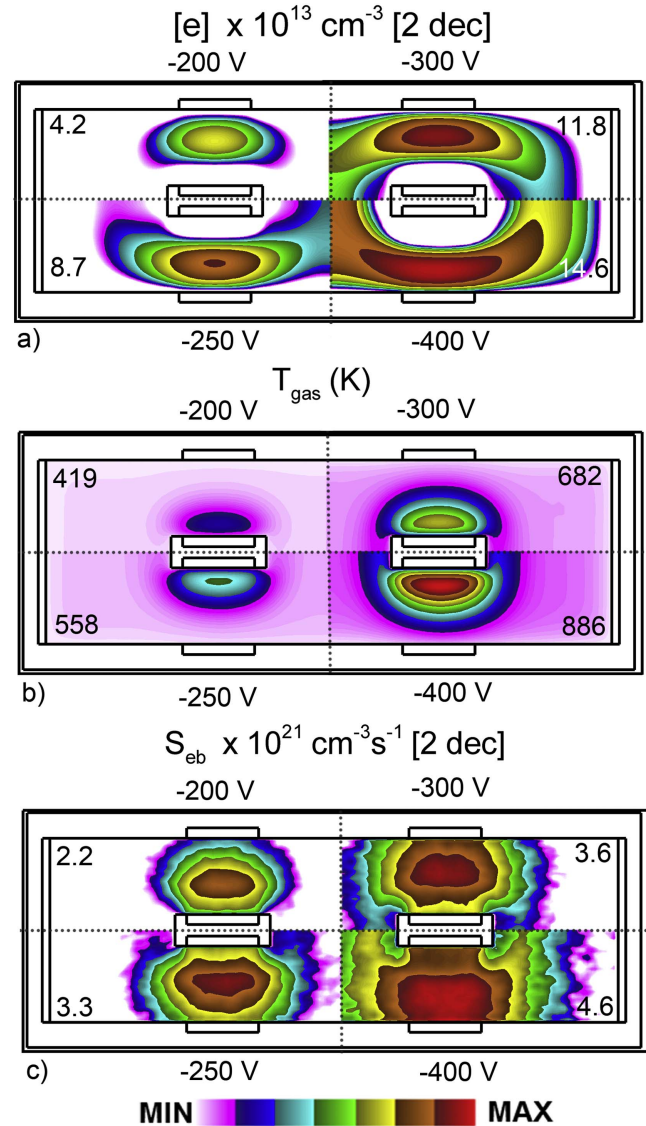


**Figure 6.** The distribution of (a) electron density, (b) gas temperature and (c) source of ionization by secondary emitted electrons from cathode for different peak pulse voltages. In the  $2 \times 2$  array, the values are essentially the same in each cell and so only one cell is shown for each voltage.

nearly 900 K for an applied potential of  $-400 \text{ V}$ . In the base case, some amount of rarefaction is helpful in maximizing ionization by secondary electrons. However, the increasing gas rarefaction with increasing voltage ultimately limits the efficiency of this ionization. As rarefaction increases with voltage, both the mean free path of secondary electrons and their energy increase. With the ionization cross section for argon peaking at about 120 eV, even in the absence of rarefaction, the mean free path of secondary electrons accelerated to the cathode fall voltage increases as the voltage increases. With rarefaction, there is an additional lengthening of the mean free path. This lengthening of the mean free path beyond the cathode–anode gap is reflected by the shift in the maximum of the ionization by secondary electrons from the middle of the gap at  $-200 \text{ V}$  to adjacent to the anode at  $-400 \text{ V}$ . At the higher voltage, the majority of secondary electrons are intercepted by the anode.

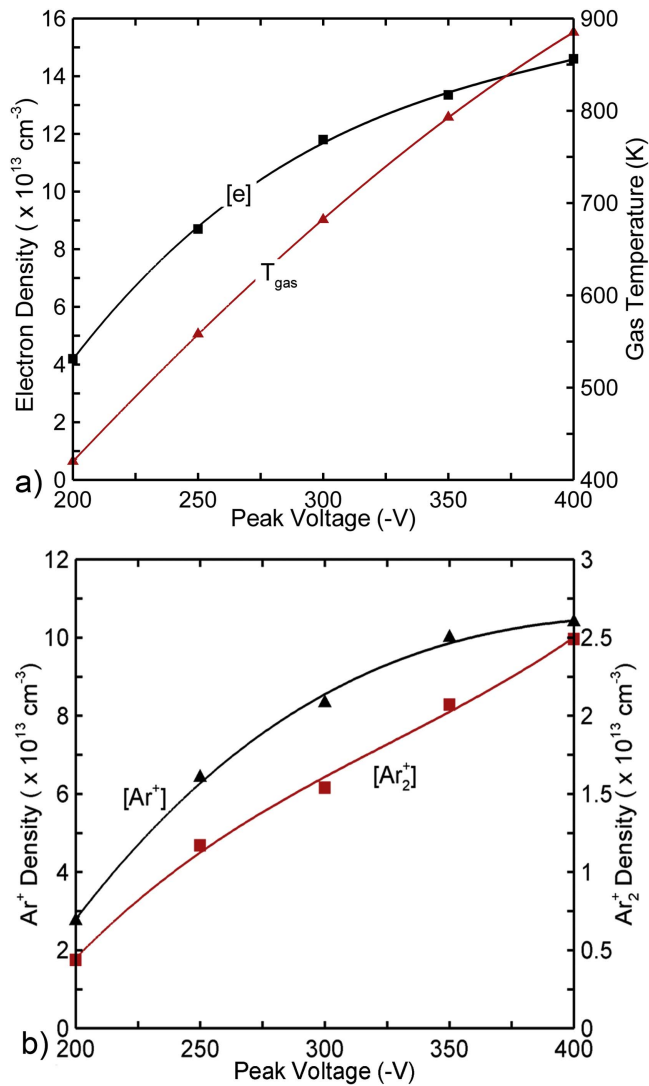


**Figure 7.** Plasma properties as a function of peak voltage. (a) Electron density and gas temperature. (b) Densities of  $\text{Ar}^+$  and  $\text{Ar}_2^+$ .

The higher gas temperature produces additional rarefaction near the cathode and additional compression of the gas in the periphery of the device. As the voltage increases, the balance between  $\text{Ar}^+$  and  $\text{Ar}_2^+$  trends towards  $\text{Ar}_2^+$  due to this increase in gas density in the periphery of the device. The higher gas density produces more  $\text{Ar}_2^+$ , which is produced through both associative ionization of high lying levels of Ar and by three-body association reactions of  $\text{Ar}^+$ .

### 3.2. Gas pressure

The electron momentum transfer collision frequency is an important property that influences the performance of an electromagnetic wave controlling plasma material. The most direct method of controlling the electron collision frequency is varying pressure. The electron density and secondary electron ionization as a function of pressure (30–80 Torr) are shown in figure 8. (Note both the electron density and the secondary electron ionization sources are individually normalized in order to show the gradient of electron densities and

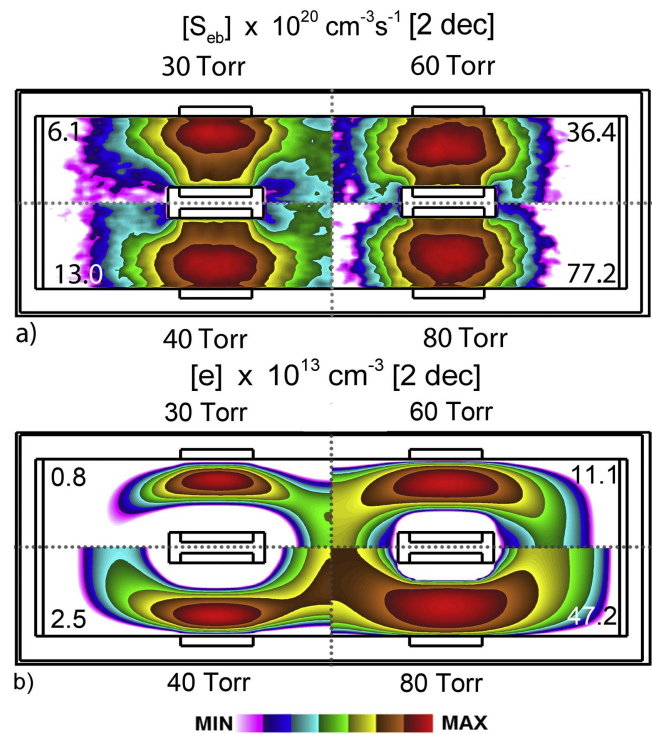


**Figure 8.** Plasma properties for argon pressures of 30, 40, 60 and 80 Torr. (a) Source of ionization due to secondary electrons and (b) electron density. In the  $2 \times 2$  array, the values are essentially the same in each cell and so only one cell is shown for each pressure.

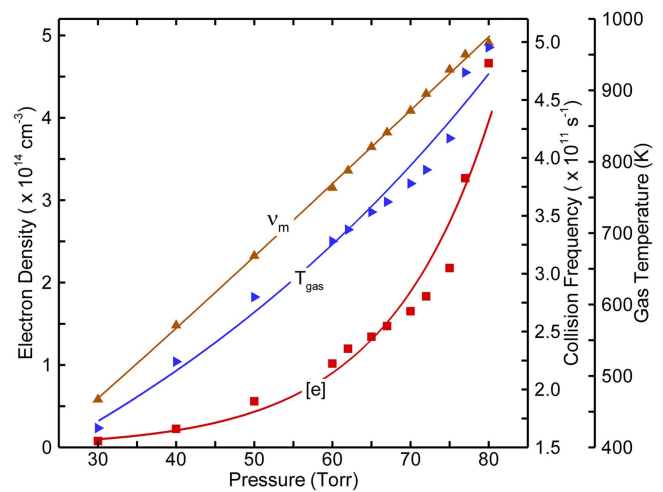


**Figure 9.** Electron momentum transfer collision frequency, gas temperature and electron density for argon pressures of 30–80 Torr.

secondary electron ionization sources for different pressures.) Correlations of collision frequency, gas temperature and electron density with pressure are shown in figure 9. The data in figure 9 are peak values at the end of the pulse at 30 ns. The momentum transfer collision frequency increases nearly linearly with pressure (from  $1.9 \times 10^{11} \text{ s}^{-1}$  at 30 Torr to  $5.0 \times 10^{11} \text{ s}^{-1}$  at 80 Torr), and so changes in the electron energy distribution with pressure has a nominal effect on collision frequency for these conditions. With the increase of the pressure, the stopping power for secondary electrons increases while rates of diffusion decrease. The peak electron



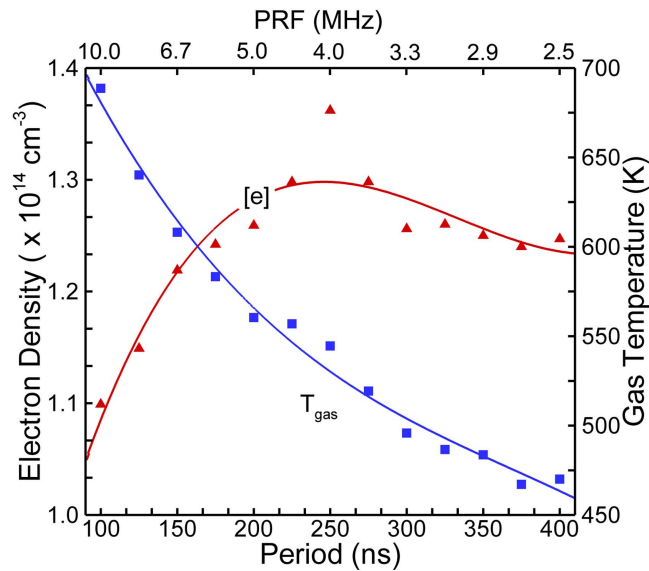


**Figure 10.** Electron density and gas temperature for pulse repetition frequencies (PRF) of 10–2.5 MHz (period of 100–400 ns). The power-on period is fixed at 30 ns.

density increases by a factor of 60 from 30 to 80 Torr to a maximum value of  $4.7 \times 10^{14} \text{ cm}^{-3}$ . Increasing pressure shortens the stopping distance for secondary electrons, until the beam ionization rate is maximum at the edge of cathode fall. This increase in ionization rate gives rise to an ion density also peaking near the edge of the cathode fall, which in turns optimizes ion loss to the cathode and additional secondary emission. This positive feedback produces an electron density that nonlinearly increases with pressure, resembling the behavior of current as a function of pressure in the normal glow. (In a classical dc normal glow discharge, current density increases with the square of pressure [26].) A counter-intuitive result is that the plasma becomes more spatially uniform with increasing pressure. This trend results from the thickness of the cathode fall decreasing with increasing pressure due to the increase in plasma density and increase in collision frequency.

### 3.3. PRF and duty cycle

The properties of the MA were investigated as a function of pulse repetition rate (PRF) and duty cycle (DC). While maintaining the pressure at 60 Torr and voltage at  $-300 \text{ V}$ , the PRF was varied from 10 MHz (100 ns period) to 2.5 MHz (400 ns period) while maintaining the voltage pulse length at 30 ns. This resulted in the duty cycle decreasing from 30% to 7.5%. The resulting maximum electron density and gas temperature are shown in figure 10. Since the peak power deposition during the pulse remains nearly constant, the time average power deposition decreases with decreasing PRF, resulting in a decrease in gas temperature (680 K at a PRF of 10 MHz to 470 K at 2.5 MHz). The decrease in gas temperature results in a higher gas density in and near the cathode fall which enables a small increase in ionization by bulk electrons. The end result is a small increase in peak electron density, from  $1.1 \times 10^{14} \text{ cm}^{-3}$  for a PRF of 10 MHz to

$1.35 \times 10^{14} \text{ cm}^{-3}$  at 4 MHz. The small decrease in electron density at even lower PRF (longer period) results from a decrease in the electron and excited state densities at the beginning of the voltage pulse. These conditions then increase the energy requirements for ionization.

### 3.4. Cross-talk

The cross-talk between plasma cells is potentially a concern in MAs without internal barriers. Cross-talk is the transport of charged particles and excited states between neighboring plasmas cells, or fringing electric fields, which change the plasma properties of the neighboring cell. To investigate the likelihood for cross-talk, voltage was sequentially applied to each plasma cell in  $2 \times 2 \text{ MA}$  in a counter-clockwise sequence. This sequencing of voltage is expected to change the cross-talk between cells compared to the simultaneous application of voltage. Using the base case conditions at 60 Torr with a pulsed period of 100 ns for all cells, the individual voltage pulses start at 10, 30, 50 and 70 ns from the top left cathode in counter-clockwise sequence. The resulting electron density is shown in figure 11 for times at which the voltage is maximum for each cell, and should be compared to figure 2(a) for the simultaneous pulsing. The relative, instantaneous magnitude of voltage for each cell is indicated by the thickness of the cathode fall. The electron densities in each cell are only nominally different than those for simultaneous pulsing, which indicates that cross-talk during the voltage pulses is not particularly important, or that the cross-talk that does occur is on time scales that are longer than the interpulse period. This cross-talk between cells is somewhat minimized by the ionization by secondary electrons for each cell, which is well confined to the volume between the electrodes of that cell.

Although cross-talk on the timescale of the voltage pulse is small, there may still be cross-talk on longer timescales due to diffusion of excited states between cells, and due to the details of the geometrical layout. To investigate these dependences, several different geometries were used, as shown in figure 12. The first geometry is a  $4 \times 2$  array with cathodes confined to the inner electrodes. The second is a  $3 \times 3$  array with alternating cathodes and anodes. The electron and  $\text{Ar}(1s_5)$  metastable densities for the  $4 \times 2$  array with simultaneous voltage pulses are shown in figure 13. The center electrodes in the column are anodes. The extension of the cathode falls towards the four corners results in confinement of the bulk plasma towards the central column of anodes and in particular, the center of the MA. This is an example of electrostatic cross-talk, which results from the geometrical asymmetries in the  $4 \times 2$  array compared to the  $2 \times 2$  array. With the expansion of the cathode falls in the four corners, there is a maximum in plasma potential in the center of the MA, producing a maximum in plasma density. In spite of the geometrical asymmetries, the peak plasma densities for each cell are essentially the same albeit with spatial inhomogeneities resulting from the asymmetric electrostatic potential. Since the  $\text{Ar}(1s_5)$  densities do not directly respond to the electrostatic potentials, their spatial distributions and peak densities are more uniform than



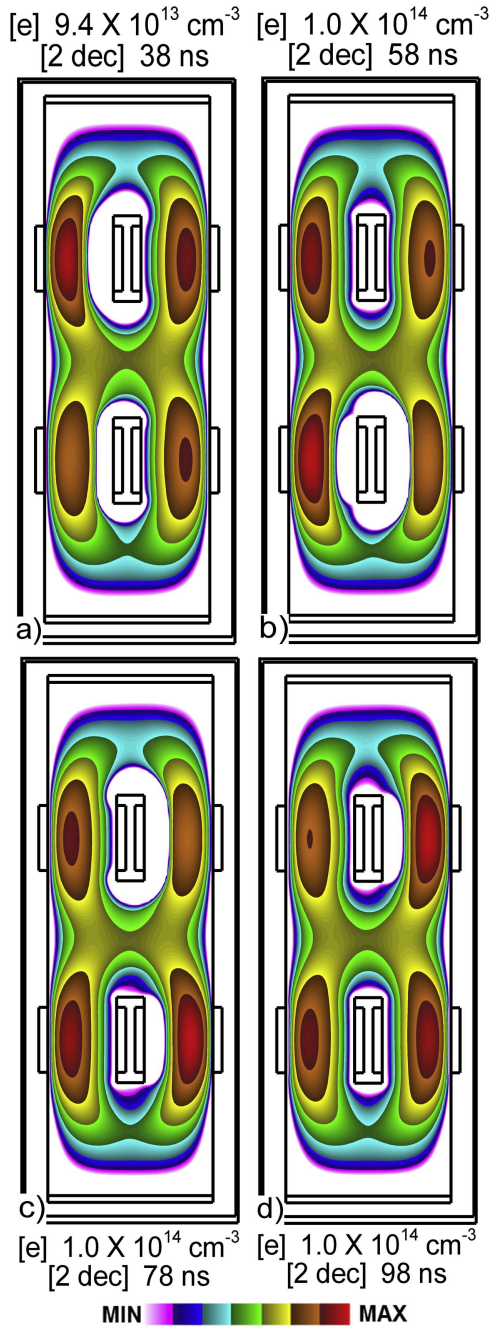


**Figure 11.** Electron densities at 60 Torr while pulsing the voltage on different electrodes at different times. (a) Top left electrode pulsed at 30 ns. (b) Bottom left electrode at 50 ns, (c) bottom right electrode at 70 ns, (d) top right electrode at 90 ns.

the electron densities. The diffusion of the  $\text{Ar}(1s_5)$  to the center of the MA in part contributes to the higher plasma density at that location by enabling more efficient multistep ionization.

In the absence of barriers, it is difficult to completely eliminate cross-talk, particularly due to transport of excited states between cells which does not directly respond to electrical forces. In pure argon plasmas, even at moderate pressures, the lifetimes of metastable states,  $\text{Ar}(1s_5, 1s_3)$  and trapped resonant states,  $\text{Ar}(1s_4, 1s_2)$  are long enough to allow their diffusive transport between cells, as seen in the  $4 \times 2$  array. As multistep ionization of, for example,  $\text{Ar}(1s_5)$  has a

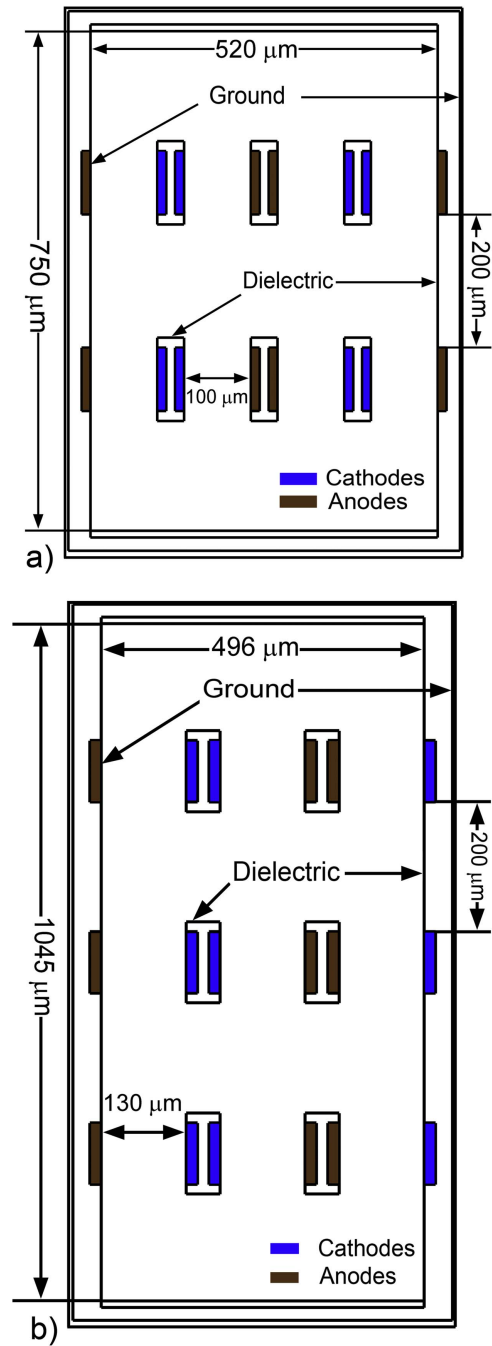


**Figure 12.** Geometries for (a)  $2 \times 4$  array and (b)  $3 \times 3$  array.

threshold energy of only 4.45 eV, the presence of even a small density of argon excited states can decrease the ignition threshold for sustaining the plasma in a given cell. In this case, cross-talk due to the exchange of  $\text{Ar}^*$  can be helpful in the ignition process of adjacent cells. As shown by the electron densities in figure 14(a) and  $\text{Ar}(1s_5)$  densities in figure 15(a), the ignition of the microplasma starts from the seeding of excited states of Ar by cross-talk between cells. (The dimensions for this layout are shown in figure 12(b).) For this  $3 \times 3$  array, the top left cathode is pulsed with a peak voltage of  $-300$  V while the other cathodes are pulsed with a peak voltage of  $-250$  V. The conditions are otherwise the same as for the base case. The geometrical arrangement of

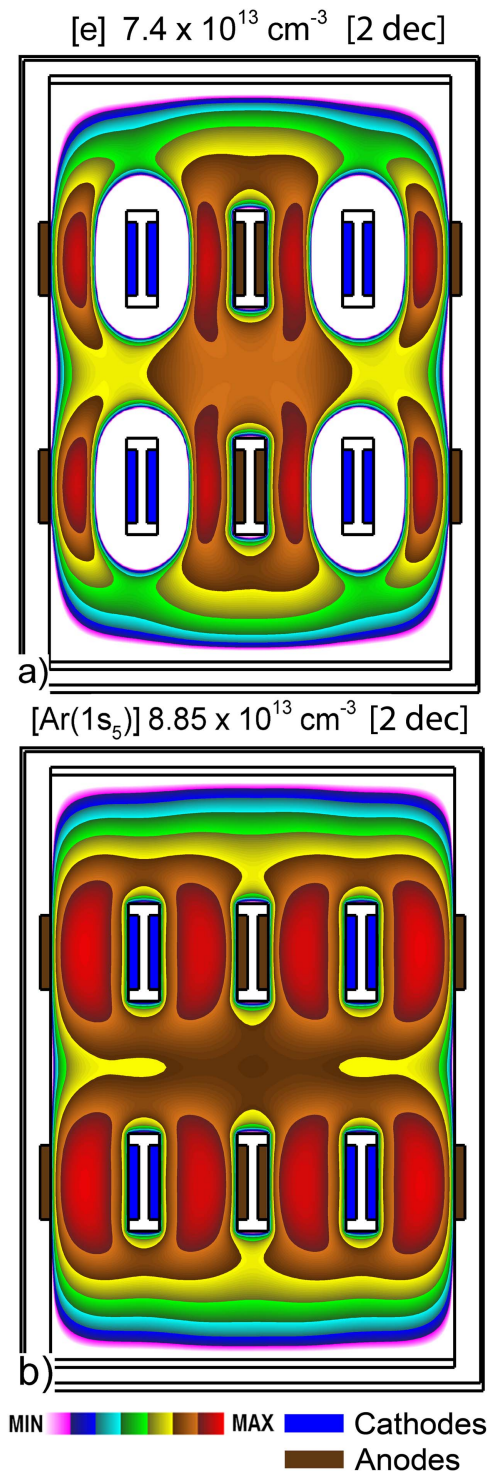


**Figure 13.** The spatial distribution of (a) electron density and (b) Ar(1s<sub>5</sub>) density in a 2 × 4 array.

electrodes results in all cells being essentially identical. Electron and Ar(1s<sub>5</sub>) densities are shown during or after the 4th, 10th, 15th, 18th and 20th pulse.

At the start of pulsing, only the cell having a −300 V bias is able to sustain a plasma. A plasma cannot be sustained with a −250 V bias in the absence of pre-ionization or a pre-existing excited state density. So for the first four pulses, only the top left cell with the −300 V bias produces plasma.

However, as Ar<sup>\*</sup> and electrons diffuse from the active plasma cell to the neighboring cells, the lower voltage cells are able to ignite. A wave of ignited cells then sweeps across the MA, reaching the bottom right corner after 18 pulses. In the pulse-periodic steady state, cross-talk between even the lower voltage cells enables those cells to operate at the lower voltage. Even so, in the pulse-periodic steady state, the 2.0 μs image in figure 14(a), the electron densities and spatial extent of the low-voltage cells are essentially the same. The higher voltage cell (top left) has a broader spatial extent, due to its thicker cathode fall that produces less confined electron drift. The peak values of the Ar(1s<sub>5</sub>) are essentially the same in each cell, however, the spatial extent is greater in the top-left compared to the bottom right of the MA, due to the longer time for diffusion for the earlier ignited cells.

The cross-talk between MA cells can lead to some hysteresis-like behavior. For example, the electron density is shown in figure 14(b) for the 3 × 3 array after achieving the quasi-steady state, followed by turning off the voltage in 3 cells to isolate the cell at the bottom right. (The cells that are turned off are the middle cell, and the cells to the right and bottom.) The corresponding Ar(1s<sub>5</sub>) densities are shown in figure 15(b). Over a period of 10–15 pulses, the electron density in the off-cells decreases by recombination with Ar<sub>2</sub><sup>+</sup> and by diffusion to surfaces. However, the bottom right cell continues to operate at the lower voltage in spite of now being isolated from the powered cells. A sufficient density of excited states has been generated in that cell to enable pulse-periodic operation at the lower voltage, with some assist of lower rates of charged particle diffusion loss to the neighboring, now charged, dielectric surfaces.

### 3.5. Optimizing gas mixtures

Several parameters are available to control the magnitude, spatial extent and cross-talk between MA cells. Similar investigations as just discussed were performed for other gas mixtures with the goal of increasing plasma density. In particular, the Penning mixture Ne/Xe was investigated over nearly the same parameter space as for Ar. (A Penning mixture contains at least one rare gas where the metastable state of the rare gas is able to Penning ionize the second lower ionization potential gas.) The trends for isolating cells, pressure and voltage were all essentially the same as for Ar. The major difference was the increased plasma density afforded by the Penning mixture. For example, for a Ne/Xe = 80/20 gas mixture at 80 Torr with −400 V pulses, a peak electron density of 1 × 10<sup>15</sup> cm<sup>-3</sup> was produced an order of magnitude higher than for pure Ar at 60 Torr. This increase in plasma density is enabled, in part, by the Penning ionization which makes a small contribution in pure Ar plasmas while making a dominant contribution in the Ne/Xe mechanism. The higher thermal conductivity of the Ne/Xe mixture results in a smaller increase in gas temperature, less rarefaction and so more efficient utilization of ionization by secondary electrons.

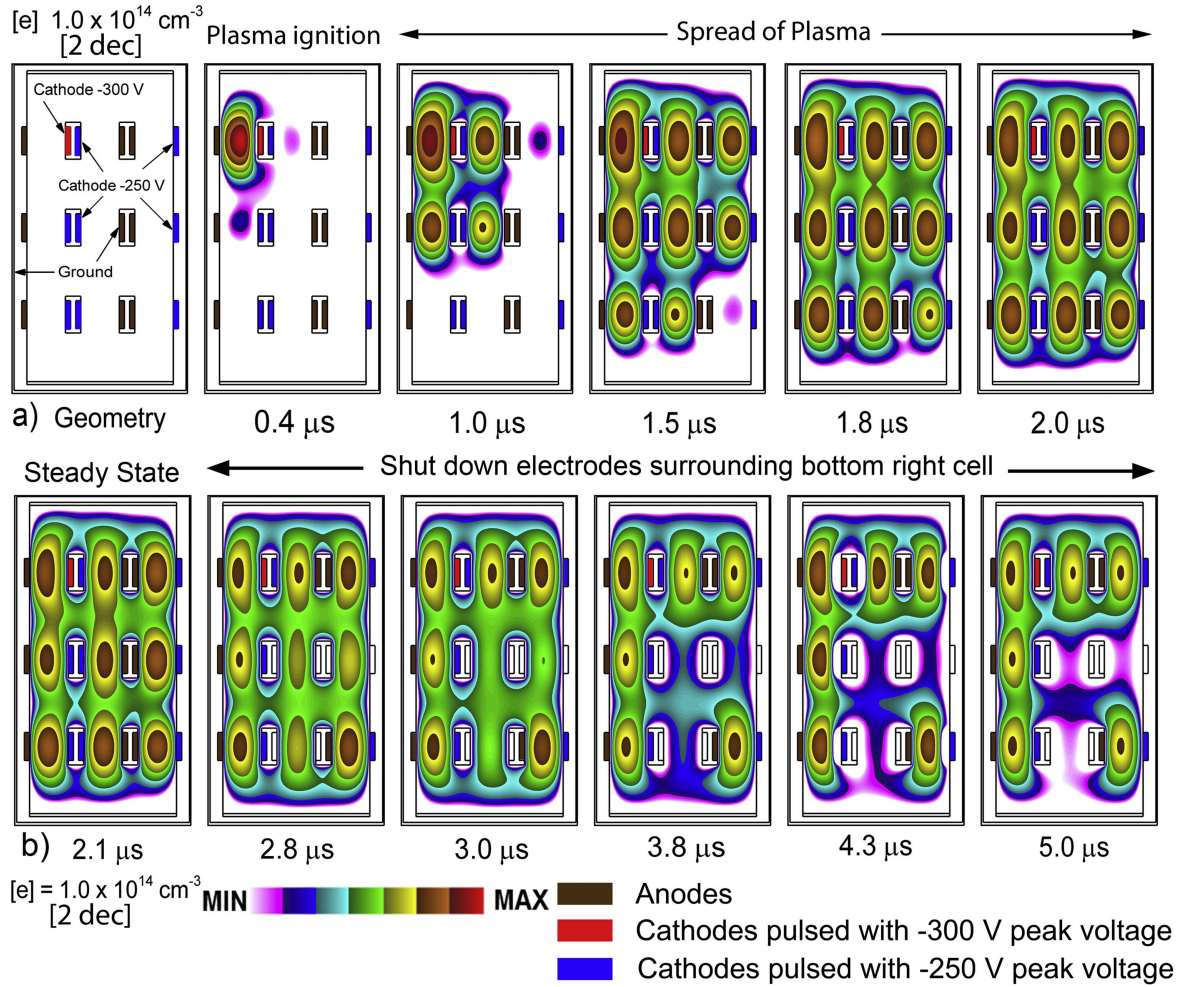


**Figure 14.** Time sequence of distribution of electron density in  $3 \times 3$  array with  $-300 \text{ V}$  applied to the top left cell and  $-250 \text{ V}$  to all other cells. (a) Sequential ignition of the entire array. (b) Evolution of electron density when turning off the voltage in cells surrounding the bottom right cell.

#### 4. Use of MAs for electromagnetics control

The control of electromagnetic wave propagation using MAs was demonstrated through simulation of the transmission of microwaves through industry standard waveguides. As described in section 2, these simulations were performed using the ANSYS Electromagnetics software package [23]. The microwave-plasma interactions addressed here are one-way. That is, the absorption of microwave radiation in the MAs was not fed back to the plasma simulations. The results shown here are then a small-signal limit.

The first demonstration uses the WR-42 waveguide having dimensions of  $10.668 \text{ mm} \times 4.318 \text{ mm} \times 75 \text{ mm}$  (a few times the wavelength) and which support EM waves of 18–26.5 GHz [27]. Test cases were performed to validate the choice of mesh and input parameters by reproducing the theoretical cut-off frequency for this waveguide at 14 GHz. The subsequent simulations were performed at 20 GHz. A  $4 \times 10$  MA composed of cylindrical plasma elements was inserted in the center of the waveguide. The radius of each MA element was  $400 \mu\text{m}$  with a thickness of 1 mm so that the plasma array can have an observable influence on the incident

EM wave with the plasma properties considered in this paper. Conceptually, the 1 mm thickness can be produced by stacking several MA layers. The entire structure is shown in figure 16(a).

For demonstration purposes, we used conditions for the Ne/Xe plasma at 80 Torr with a cycle average electron density of  $n_e = 7.2 \times 10^{14} \text{ cm}^{-3}$  and electron collision frequency  $\nu_m = 1.5 \times 10^{11} \text{ s}^{-1}$ . The parameter of interest is the transmission coefficient for the relative power of the wave exiting the waveguide compared to the power entering the waveguide. The waveguide mode first investigated was the dominant  $\text{TE}_{10}$ , which has a maximum in the amplitude of the electric field at the center of the waveguide.

Different configurations of the MA and the resulting transmission coefficient,  $\alpha$ , are shown in figure 16. The plasma cells that are ‘on’ are shown in the dark purple—‘off’ cells are shown in the light gray. For the empty waveguide (or all plasma cells ‘off’),  $\alpha = 100\%$  (for a lossless waveguide). With all plasma cells turned on,  $\alpha = 68\%$ . If the center two columns in the MA are turned off,  $\alpha$  increases to 80%. If the center two rows are turned off (20 cells off),  $\alpha = 92\%$ . If the



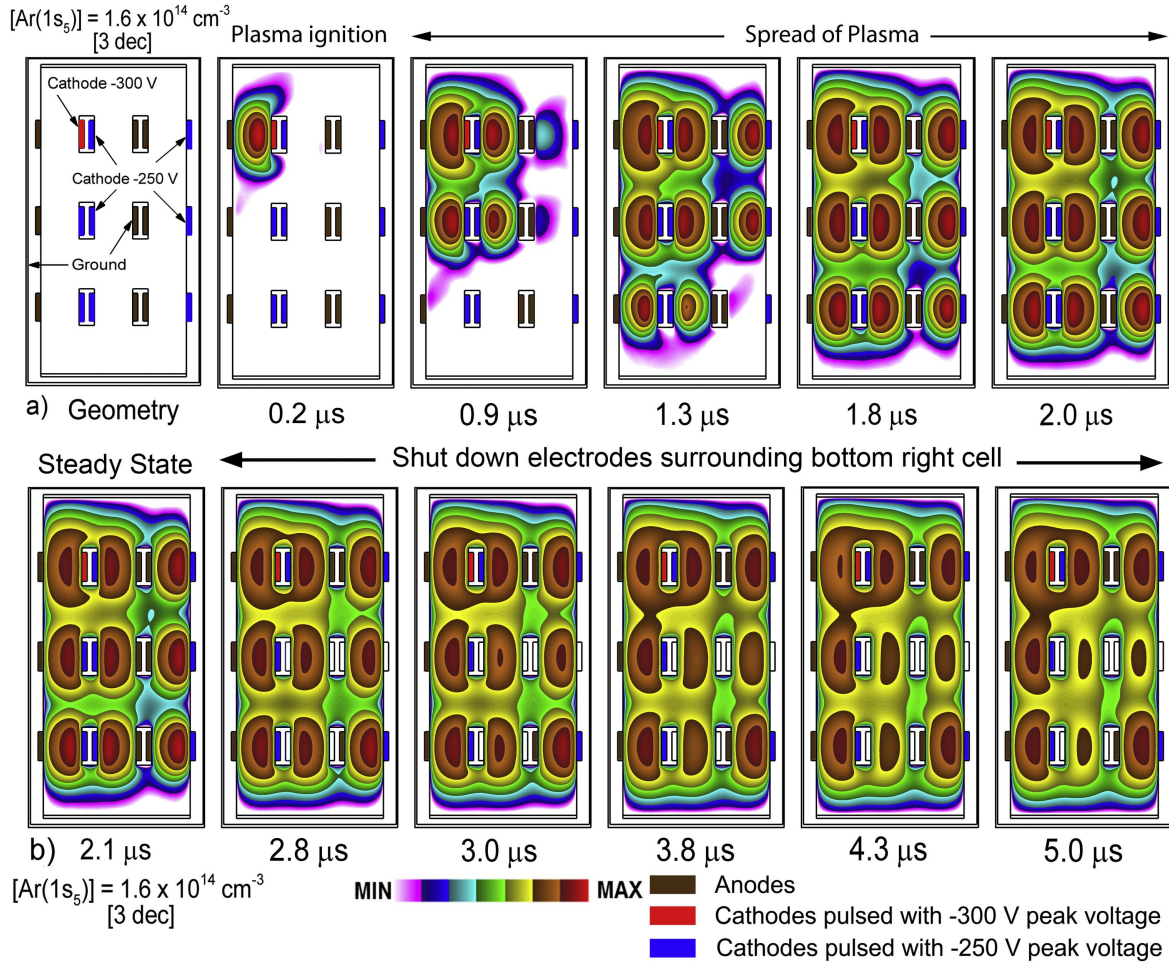


**Figure 15.** Time sequence of distribution of Ar(1s<sub>5</sub>) density in 3 × 3 array with −300 V applied to the top left cell and −250 V to all other cells. (a) Sequential ignition of the entire array. (b) Evolution of density of Ar(1s<sub>5</sub>) when turning off the voltage in cells surrounding the bottom right cell.

same number of cells are turned off, but in alternating columns,  $\alpha = 84\%$ .

The dependence of transmission coefficient on the layout of the on-plasma cells is in large part determined by the mode structure of the wave. The amplitude of the TE<sub>10</sub> mode is largest in the center of the waveguide, decreasing as a sine-function towards the surfaces in the vertical dimension. Plasma cells that overlap with the maximum in the amplitude of the guided wave have a disproportionate influence on the transmission properties of the wave, thereby accounting for the increase in transmission when turning off the plasma cells that overlap the maximum amplitude (figure 16(c)). For example, with the same number of off cells, the arrangement in figure 16(d) which has off cells coinciding with the maximum in the electric field in the lateral direction has a larger transmission coefficient than the arrangement in figure 16(e), where plasma on the cells intersects with the maximum amplitude of the wave. The plasma cells on the edge of the waveguide are less influential on the transmission coefficient, being either on or off, because the amplitude of the wave is smaller near the top and bottom walls of the waveguide.

To further demonstrate the mode-dependencies on transmission through the waveguide having a MA, the TE<sub>20</sub>

mode was investigated with the same WR-42 waveguide and MA geometry. (The TE<sub>20</sub> mode has a zero crossing at half-height in the vertical direction.) In this case, the frequency of the propagating wave is 45 GHz to exceed the 28.1 GHz cutoff frequency of the TE<sub>20</sub> mode. With all of the plasma cells turned on,  $\alpha = 32\%$ . With the two center columns turned off, as in the structure shown in figure 16(c),  $\alpha$  increases only nominally to 33% as this region corresponds to the minimum in the electric field. Turning off the plasma cells in the two center rows increases transmission to 72%, while alternating columns of on-off plasma cells reduce the transmission to 45%.

This dependence on the spatial arrangement of off-and-on cells is further demonstrated using a WR-12 waveguide having dimensions 1.549 mm × 3.3099 mm × 17 mm, which sustains a frequency range of 60–90 GHz for the dominant TE<sub>10</sub> mode. Transmission coefficients were computed for a frequency of 65 GHz with a 7 × 15 MA placed at the center of the waveguide, as shown in figure 17(a). Each element of the MA is 80  $\mu\text{m}$  in radius and 0.5 mm in thickness. The plasma properties are  $7.2 \times 10^{14} \text{ cm}^{-3}$  electron density and  $1.5 \times 10^{11} \text{ s}^{-1}$  collision frequency. Plasma cells were turned on column by column (with 15 cells in one row)



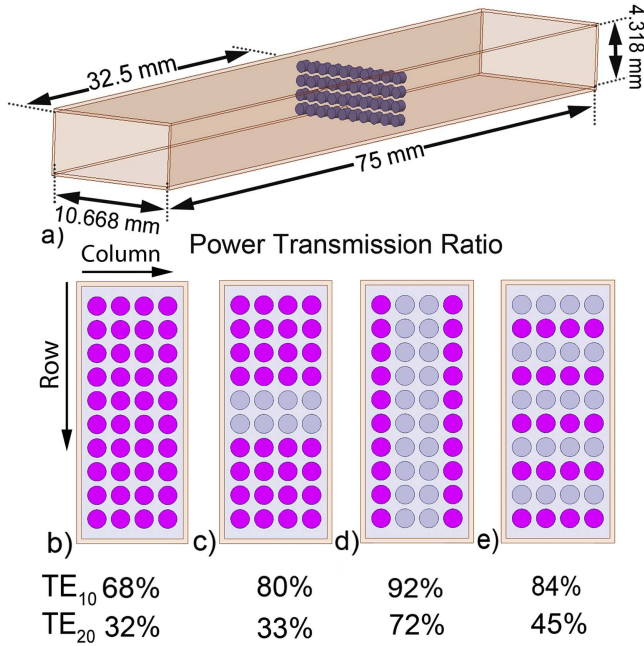


**Figure 16.** Transmission through a microwave guide with an embedded  $4 \times 10$  MA. (a) Geometry for WR-42 waveguide, and (b) TE<sub>10</sub> and TE<sub>20</sub> mode power transmission coefficients for different MA patterns. Purple (dark) denotes a plasma-on cell. Gray (light) denotes a plasma-off cell.

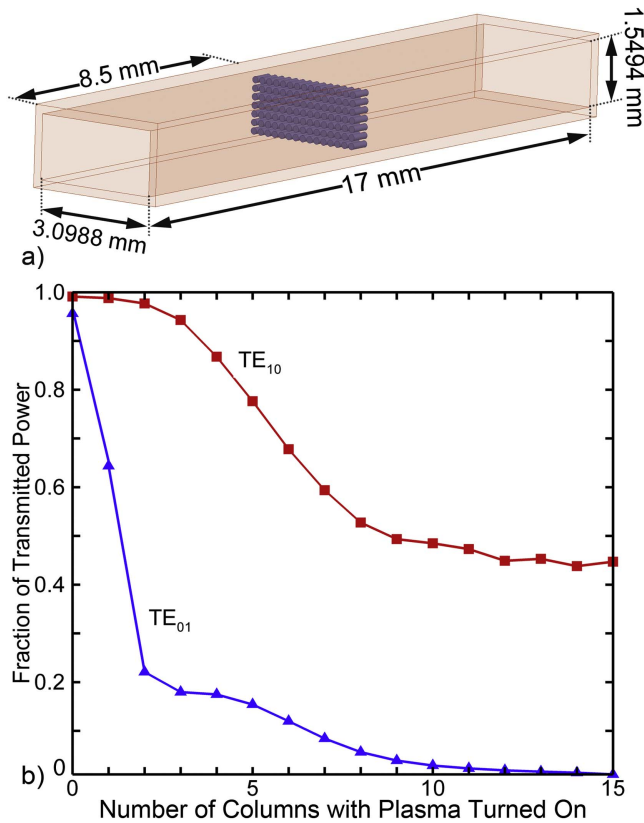


**Figure 17.** Transmission through a microwave guide with an embedded  $7 \times 15$  MA. (a) Geometry for WR-12 waveguide and (b) TE<sub>10</sub> and TE<sub>01</sub> mode power transmission coefficients for successively turning on the 15 columns the MA each having 7 cells.

from the left to the right of the waveguide. The resulting power transmission ratio  $\alpha$  of the TE<sub>10</sub> mode is shown in figure 17(b) as a function of the number of plasma columns turned on. The power transmission has a small decrease when turning on the first 4–5 columns of plasma cells as this region is where the electric field is low. Between turning on 4 and 10 columns of plasma cells,  $\alpha$  decreases from 95% to 50% as the on-cells begin to overlap with the maximum in the electric field. Turning on the last five columns of plasma cells produces an additional decrease of only 5%, to a final value of  $\alpha = 45\%$  for the fully on MA.

The second mode investigated for the WR-12 waveguide is the TE<sub>01</sub> mode. The cutoff frequency of this mode is 96.8 GHz. A 100 GHz wave, close to the cutoff frequency, was modeled. The power transmission coefficient of the TE<sub>01</sub> mode with number of columns of MA turned on is shown in figure 17(b). Since the TE<sub>01</sub> mode is not the dominant mode of rectangular waveguide and the frequency is close to the cutoff, even a small absorption in space can produce a significant decrease in overall transmission. The transmission ratio  $\alpha$  decreases from nearly 100% to approximately 20% when the first two columns of plasma are turned on. Between turning on 3–15 columns of plasma, the transmitted power from the TE<sub>01</sub> mode decreases almost linearly because the field is uniform along the direction of the 3.1 mm edge.

## 5. Concluding remarks

In this paper, the scaling of MAs consisting of plasma elements having dimensions of hundreds of microns was investigated with the goal of implementing such MAs as controlling elements of high frequency electromagnetic waves. For such applications, the individual MA elements may not have physical barriers, and so there may be interactions (cross-talk) between plasma cells. Pulsed operation of MAs sustained in up to 80 Torr of argon consisting of up to  $3 \times 3$  elements produce plasma densities of  $10^{14} \text{ cm}^{-3}$ . In Ne/Xe Penning mixtures, the plasma density is as high as  $10^{15} \text{ cm}^{-3}$ . Gas heating in sealed MA cavities redistributes the gas density, which then impacts the range of secondary electrons accelerated in the cathode fall. For MA elements that are sustained by ionization by secondary electrons confined to the cathode–anode gap, there was little cross-talk between active cells. However, the startup of plasma cells was sensitive to cross-talk resulting from the diffusion of excited states from distant cells which enabled startup at lower voltages. Once started, the MAs displayed some amount of hysteresis behavior, where individual cells at low voltage were sustained even when isolated from the high voltage cells.

The potential for EM control of MAs having plasma properties predicted by the model was numerically investigated by computing transmission coefficients for high frequency EM waves through standard waveguides having MAs

at their center. Transmission coefficients can be tuned based on the arrangement of active MA plasma cells, and their overlap with the amplitude of the local electric field.


## Acknowledgments

This work was supported by the Air Force Office of Scientific Research (FA9550-14-1-0371), Department of Energy Office of Fusion Energy Sciences (DE-SC0001319, DE-SC0014132) and the National Science Foundation (PHY- 1519117, CHE-1124724).

## ORCID iDs

Chenhui Qu  <https://orcid.org/0000-0002-8300-9398>

Peng Tian  <https://orcid.org/0000-0001-5042-6219>

Abbas Semnani  <https://orcid.org/0000-0003-4284-3914>

Mark J Kushner  <https://orcid.org/0000-0001-7437-8573>

## References

- [1] Sakai O, Naito T and Tachibana K 2010 *Phys. Plasma* **17** 057102
- [2] Kourtzanidis K, Pederson D M and Raja L L 2016 *J. Appl. Phys.* **119** 204904
- [3] Singh P K, Hopwood J and Sonkusale S 2014 *Sci. Rep.* **4** 5964
- [4] Sakai O and Tachibana K 2012 *Plasma Source Sci. Technol.* **21** 013001
- [5] PanneerChelvam P, Raja L L and Upadhyay R R 2016 *J. Phys. D: Appl. Phys.* **49** 345501
- [6] Sakai O, Nakamura Y, Iwai A and Iio S 2016 *Plasma Sources Sci. Technol.* **25** 055019
- [7] Smith D R, Pendry J B and Wiltshire M C K 2004 *Science* **305** 788
- [8] Shalaev V 2007 *Nat. Photon.* **1** 41
- [9] Iwai A, Nakamura Y, Bambina A and Sakai O 2015 *Appl. Phys. Express* **8** 056201
- [10] Sakai O 2011 *J. Appl. Phys.* **109** 084914
- [11] Naito T, Sakai O and Tachibana K 2008 *Appl. Phys. Express* **1** 066003
- [12] Wang B and Cappelli M A 2016 *Appl. Phys. Lett.* **108** 161101
- [13] Wang B and Cappelli M A 2016 *AIP Adv.* **6** 065015
- [14] Semnani A, Missen Z V, Macheret S and Peroulis D 2016 Gas discharge tube-based variable RF attenuator *IEEE Wireless and Microwave Technology Conf. (Clearwater, FL)*
- [15] Hoskinson A R and Hopwood J 2014 *Plasma Sources Sci. Technol.* **23** 015024
- [16] Monfared S K, Hoskinson A R and Hopwood J 2013 *J. Phys. D: Appl. Phys.* **46** 425201
- [17] Miura N and Hopwood J 2011 *J. Appl. Phys.* **109** 113303
- [18] Boeuf J P 2003 *J. Phys. D: Appl. Phys.* **36** R53
- [19] Eden J G and Park S-J 2014 Microcavity and microchannel plasmas: general characteristics and emerging applications *Complex Plasmas: Scientific Challenges and Technological Opportunities (Springer Series on Atomic, Optical and Plasma Physics vol 82)* ed M Bonitz et al pp 373–98
- [20] Eden J G, Braun P V, Park S-J, Yang H J and Sun P Control of electromagnetic energy with spatially periodic microplasma devices *US Patent Application* 20170207523 A1
- [21] Kushner M J 2009 *J. Phys. D: Appl. Phys.* **42** 194013
- [22] Song S-H and Kushner M J 2012 *Plasma Sources Sci. Technol.* **21** 055028
- [23] ANSYS® Electromagnetics, Release 16.1 <http://ansys.com/products/electronics/ansys-hfss>
- [24] Tian P and Kushner M J 2015 *Plasma Sources Sci. Technol.* **24** 034017
- [25] Bohm C and Perrin J 1993 *Rev. Sci. Instrum.* **64** 31
- [26] Fridman A and Kennedy L A 2004 *Plasma Physics and Engineering* (New York: Taylor and Francis) ch 7
- [27] Anderson T N 1956 Rectangular and ridge waveguide *IRE Trans. Microw. Theory Tech.* **MTT-4** 201